

Superresolution based on coherent thermal radiation with selective information

Duan-Hsin Huang¹ · Chih-Wei Chang^{1,2}

Received: 30 July 2024 / Accepted: 3 February 2025

Published online: 13 February 2025

© The Author(s) 2025 [OPEN](#)

Abstract

We reexamine superresolution methods that may have been overlooked by previous optical microscopy techniques. For a one-dimensional (1D) system, we show that maximizing the information capacity of an imaging system is not a necessary condition for surpassing the Abbe diffraction limit. Specifically, the spatial resolution of two coherent emitters can go beyond the Abbe diffraction limit if an appropriate information zone, but not the full information zone, is selected for far-field imaging. Based on this principle, we show that $\lambda/2.6$ superresolution can be easily achieved for two coherent thermal radiative sources with a sufficiently large phase difference. Similar effects can be found for a 1D array of thermal radiative sources coupled by surface phonon polaritons. Introducing a dielectric microsphere into the system can further enhance the phase difference among the radiative sources, achieving superresolution better than $\lambda/4$. The concept and method presented here can be implemented to enhance the spatial resolution of thermal imaging.

Keywords Superresolution · Thermal radiation · Optical microscopy · Phonon-polariton

1 Introduction

Although an optical image can serve a wide range of applications, a fundamental description of its purpose is to deliver the required information, but not the full information, of an investigated object correctly. On the other hand, because no physical quantity measurement would give infinitely precise results in the presence of noise, an optical system that transmits the required information via light must be limited by bandwidth and noise. Thus, an optic microscope can be regarded as a special instrument resolving the problem of signal recovery. Mathematically, a general case of signal recovery can be expressed as the Fredholm integral equation of the first kind,

$$\int_a^b K(x, y) f_0(y) dy = F_0(x) \quad (1)$$

where $f_0(y)$ is the unknown function to be determined, $F_0(x)$ is the result of the measurement, and $K(x, y)$ is the point spread function (PSF). However, the general solution of Eq. (1) is difficult to obtain, and various efforts are being devoted to finding special solutions for it [1, 2]. From this point of view, Rayleigh's criteria of the resolution limit of a microscope is

Supplementary Information The online version contains supplementary material available at <https://doi.org/10.1186/s11671-025-04209-7>.

✉ Chih-Wei Chang, cwchang137@ntu.edu.tw | ¹Center for Condensed Matter Sciences, National Taiwan University, Taipei 10617, Taiwan. ²Center of Atomic Initiative for New Materials (AI-MAT), National Taiwan University, Taipei 10617, Taiwan.



an example that provides a simplified solution for Eq. (1) by finding an effective width (Δ) of $K(x,y)$ at the far field ($y \gg \Delta$) to obey

$$|K(x,y)/K(x,0)| \gg 1 \quad (2)$$

Historically, Shannon formulated the fundamental limit of the maximum information that can be transmitted in a noisy channel without explicitly solving Eq. (1). The application of the Shannon theorem to an optic microscope has been discussed in many works [3–11]. It imposes a fundamental limit of spatial resolution (Δ) [10]:

$$\Delta = \frac{\lambda}{2} \frac{1}{\log_2 \sqrt{1 + 2SNR_{eff}}} \quad (3)$$

where SNR_{eff} is the effective signal-to-noise ratio of the detector, and λ is the wavelength of the incident light. Considering a practical detector with $SNR_{eff} = 1000$, Eq. (3) gives $\Delta < \lambda/10$, which is much better than the Abbe's diffraction limit $\Delta \sim \lambda/2$. The result implies that there is still much room for improvement, even though Eq. (1) is difficult to solve. Recently, with the advancement of neural networks, more improvements in Δ can now be achieved even without explicit algorithms [11, 12].

Because of the invariance of information capacity in an imaging system [13–16], a lot of works have been developed to get more information in a desired dimension while compromising unwanted information in another dimension [11]. The far-field superresolution techniques, such as structural illumination [17], super-oscillation lens [18], and hyperlens [19, 20], extend the spatial bandwidth beyond the cut-off frequency of Eq. (2) through advanced fabrication processes to create specialized lenses. In addition, post-image-processing employing assumptions of sparsity or prior knowledge of samples can further aid information retrieval [12, 21, 22]. We also note that although the maximum information capacity of an imaging system sets the ultimate Δ , the superresolution techniques discussed above have implicitly assumed that better Δ can always be achieved when the maximum available information of the system is used. The implicit assumption suggests that whenever the setup is available, a microscope user should always collect as much light as possible at the far field to achieve better spatial resolution.

The implicit assumption may not always be correct when the coherence of light is introduced to an optical system. In this paper, we present a counterexample to the implicit assumption, demonstrating that superresolution can be achieved without utilizing the full information emitted from the sources in a one-dimensional (1D) system. We apply this new method in a 1D system to enhance the spatial resolution beyond the diffraction limit of thermal imaging when the radiative sources are coherent.

2 The principle of coherent superresolution with selective information

We first reexamine the diffraction limit using a classic example of two coherent point sources in a 1D system (separated by a distance d_0 , and immersed in a media with refractive index n) emitting lights with wavelength λ and a phase difference θ_c , as shown in Fig. 1. The minimum of the first destructive interference will occur at an angle θ , following the relation $2\pi n d_0 \lambda \sin\theta = \pi$. Similar to the classic example of resolving two incoherent sources by identifying a local intensity minimum at the far-field image, a microscope objective with numerical aperture ($NA = n \sin\theta'$, where θ' is one-half angular aperture of the objective) is able to distinguish the two emitters only when it can detect the minimum. So, we have $\sin\theta = \lambda/2nd_0 < \sin\theta'$, and the minimally resolvable distance is $d_0 = \lambda/2NA$, which is Abbe's resolution limit for two coherent emitters.

Now, consider that there is a difference between the two coherent emitters. The condition for observing the first destructive interference changes to $2\pi n d_0 \sin\theta/\lambda + \theta_c = \pi$. Correspondently, the criteria for resolving the two emitters is relaxed:

$$\frac{\lambda}{2n} \left(\frac{1}{d_0} - \frac{1}{\lambda_c} \right) < \sin\theta' \quad (4)$$

where $\lambda_c = 2\pi d_0/\theta_c$ is a characteristic length. Except for $\theta_c = 0^\circ$, now the condition for destructive interference is relaxed only at one side of the imaging plane but not the other. Thus, only half of the emitted lights are used for imaging, as shown in Fig. 1. Because information capacity increases with numerical aperture, imaging using half of the emitted light indicates a reduced and selective information capacity is used. Thus, we name the technique coherent superresolution

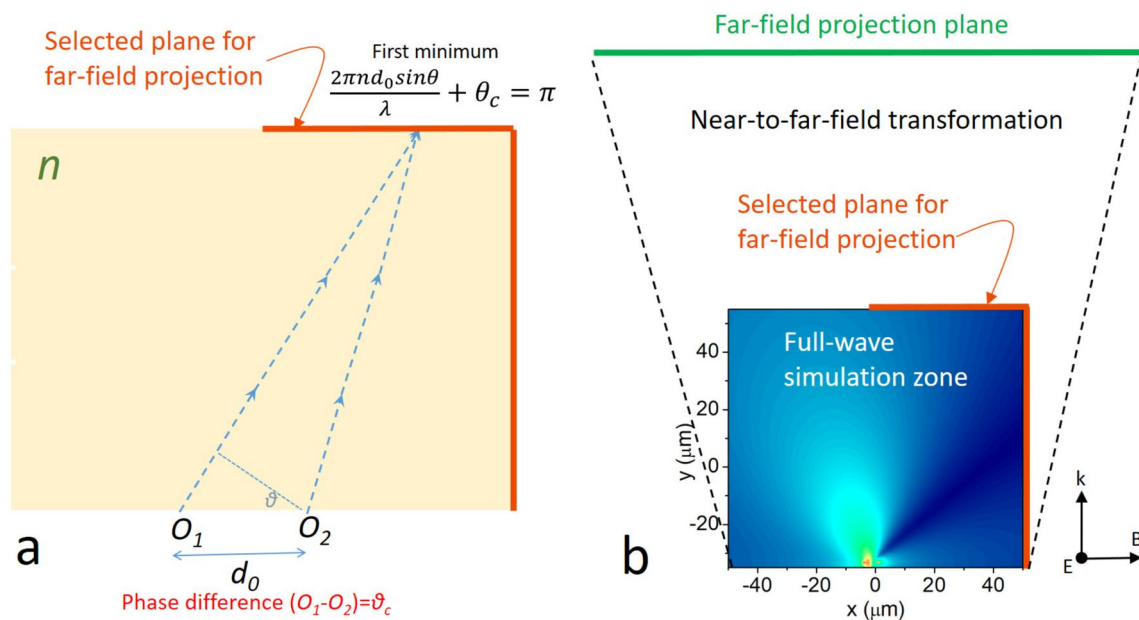


Fig. 1 The principle of coherent superresolution with selective information (CSSI). **a** When there is a phase difference (θ_c) between two coherent emitters (denoted by O_1 and O_2 , immersed in a media of refractive index n), the first minimum of the diffracted light will appear at a smaller angle (expressed by Eqs. (4) and (5)) than that of an ordinary reflective grating ($\theta_c=0$). Selecting the correct zone for imaging (the orange line) enables a far-field observer to distinguish two point sources beyond the diffraction limit, a key feature of CSSI. **b** The simulation architecture of CSSI. The emitters with polarization perpendicular to plane are located at the bottom of the full-wave simulation zone. To implement CSSI, a selected plane at the boundary of the full-wave simulation zone is chosen for transforming the near-field electromagnetic waves to the far-field. Then the information at the far-field project plane is used for creating virtual image of the objects. In our work, $n=1$ is set in our simulations

with selective information (CSSI), and it is a key factor that has been overlooked by previous works. Compared to Abbe's diffraction limit, CSSI has the minimally resolvable distance (d) that obeys:

$$\frac{1}{d} = \frac{1}{d_0} + \frac{1}{\lambda_c} \quad (5)$$

which shows that d is a harmonic mean of d_0 and λ_c . Thus, d is always smaller than d_0 or λ_c , surpassing the diffraction limit. Note that although it has been known that $\theta_c=180^\circ$ can always have an intensity minimum at the image plane [23], the concept of CSSI has not been discussed to our knowledge. Mathematically, Eq. (5) resembles many other far-field superresolution techniques, for example, two-photon imaging, structural illumination, and hyperlens. In the following, we will discuss their differences and show that Eq. (5) is a new concept of optic imaging technique.

3 Results and discussion

3.1 Comparing CSSI with other superresolution techniques

Two-photon imaging is based on the nonlinear optic phenomena that two incoming coherent lasers are up-converted by a target object and emit at higher frequencies. Thus, the outgoing light would have shorter wavelengths and better spatial resolution. The mathematical basis of the two-photon imaging is $k_1 + k_2 = k_3$ and $\omega_1 + \omega_2 = \omega_3$ (where k_i is the wave factor and ω_i is the frequency of the light). Although two-photon imaging is advantageous in detecting tissue structures 1 mm below the surface [24], its requirements of high-intensity lasers to excite the target sample have been the major drawback of its applications [25].

Structural illumination employs a shift of the frequency spectrum of a sample by illuminating it using a periodic structure with a spatial modulation frequency k_{mod} [17]. The superimposed image would have Moiré fringes that contain

information about high-frequency patterns that would otherwise not be visible. Mathematically, its principle can be expressed as $k_{in} + k_{mod} = k_{out}$ ($k_{mod} < k_{in}$). It is often used for fluorescent imaging of biological samples [26]. However, because of the need to capture 360° frequency domain, rotating the modulated pattern and computational post-processing are required [26]. Furthermore, because of the fundamental constraint $k_{mod} < k_{in}$, its spatial resolution cannot go beyond $2k_{in}$.

Hyperlens employs a sophisticated lens design that modifies its frequency contour at the Fourier space into a hyperbolic curve, extending the spatial frequency in the radial direction while compressing the azimuthal information [19, 20]. Its mathematical basis is $k_{in} + k_{mod} = k_{out}$ without the additional constraint of $k_{mod} < k_{in}$ mentioned in structural illumination [27]. Although the concept has been benefitted by the introduction of metamaterials, the fabrication difficulties have limited its applications [11].

Thus, despite the similarities in the mathematical formulation, we now understand the fundamental difference between Eq. (5) and other techniques. Unlike the two-photon imaging, CSSI does not require optical nonlinearity. Unlike structural illumination or hyperlens, the phase difference required by CSSI does not necessarily demand modulated structures. In fact, coherent light sources and selecting an appropriate zone for imaging are two important features of our technique. Although the former has been extensively investigated in literature, the latter has never been discussed to our knowledge.

3.2 Simulation of CSSI from two emitters

Although thermal radiative light sources such as incandescent light bulbs are often considered to be incoherent, employing surface phonon-polaritons as a coupling mediator to realize coherent thermal radiation has been experimentally demonstrated in various polar materials with engineered structures [28–39]. In general, artificially designed meta-surfaces can be used for controlling the dispersion relation of surface phonon-polaritons as well as the θ_c [40]. Thus, coherent thermal radiation is an ideal platform to explore our ideas. We have employed FDTD simulation using *Lumerical-FDTD* to test the concept of CSSI. We put point sources with a separation d_0 and impose a phase difference θ_c . As shown in Fig. 1b, a selected plane at the boundary of the full-wave simulation zone is used to transform the near-field electromagnetic waves into forward-propagating waves to the far-field [41]. The magnitude and phase of the angular spectrum at the far-field projection are then Fourier-transformed and backward propagated to get the intensity profile of the virtual image of the object at the far field [41]. After backward propagation, we adjust the position of the image plane to get a focused virtual image. The process will naturally give a magnified virtual image at the far field [41]. The above procedures are conducted using *Lumerical-FDTD* and have been validated experimentally [41]. Controlled simulations of incoherent imaging for two-point emitters are carried out using $\theta_c = 90^\circ$.

We have numerically simulated the system shown in Fig. 2a using two-point sources with $d_0 = 4.7 \mu\text{m}$ and $\lambda = 10 \mu\text{m}$. To quantify the resolution, we first define the visibility $= (I_{max} - I_{min}) / (I_{max} + I_{min})$ (where I_{max} and I_{min} are, respectively, the local intensity maximum and minimum of the far-field intensity profile; see supplementary information S1). To quantify the spatial resolution, we first establish the relation between the visibility and the full-width-at-half-maximum (FWHM) of two incoherent emitters and then use it to determine the effective FWHM of the images obtained by CSSI (see supplementary information S1). Figure 2b shows the relation between FWHM and visibility obtained from the deconvolution of various emission λ 's with a fixed $d_0 = 4.7 \mu\text{m}$. We find that the visibility vanishes when $\text{FWHM} = 4.83 \mu\text{m} = 1.03d_0$. In the following, we will find that the effective FWHMs obtained at different conditions can be regarded as d in Eq. (5). We choose the highest visibility in the far-field intensity profile to quantify the resolution. When $\theta_c = 80^\circ$, the far-field intensity profile at the selected imaging zone is shown in Fig. 2c. It displays two intensity peaks, correctly suggesting the presence of two emitters at the source. We also find that the two peaks show unequal intensities even though the magnitude of the two emitters is set to be equal. It is a common feature of CSSI, and it originates from the θ_c and the selected zone of imaging that causes the asymmetric intensity profile. From Fig. 2b, we find $\text{FWHM} < \lambda/2.6$ (or $\text{FWHM} = 0.82d_0$) when $\theta_c = 80^\circ$, surpassing the diffraction limit.

To prove that the coherence of the emitters and the selected information are the two key factors of CSSI, we provide two controlled simulations, one for incoherent imaging and another for coherent imaging with full information capacity, as shown in Fig. 2d, e (see supplementary information S2). Compared with Fig. 2c, we can see that neither incoherent imaging nor coherent imaging using full zone can clearly resolve the two-point sources at the far field.

We have conducted a series of simulations for various d_0 or θ_c . As shown in Fig. 3, we find that CSSI can easily go beyond the diffraction limit and correctly resolve the two emitters. Besides, increasing d_0 or θ_c would generally improve visibility. These features can be understood from Eq. (5) that the resolving power increases as θ_c increases. Furthermore, intensity

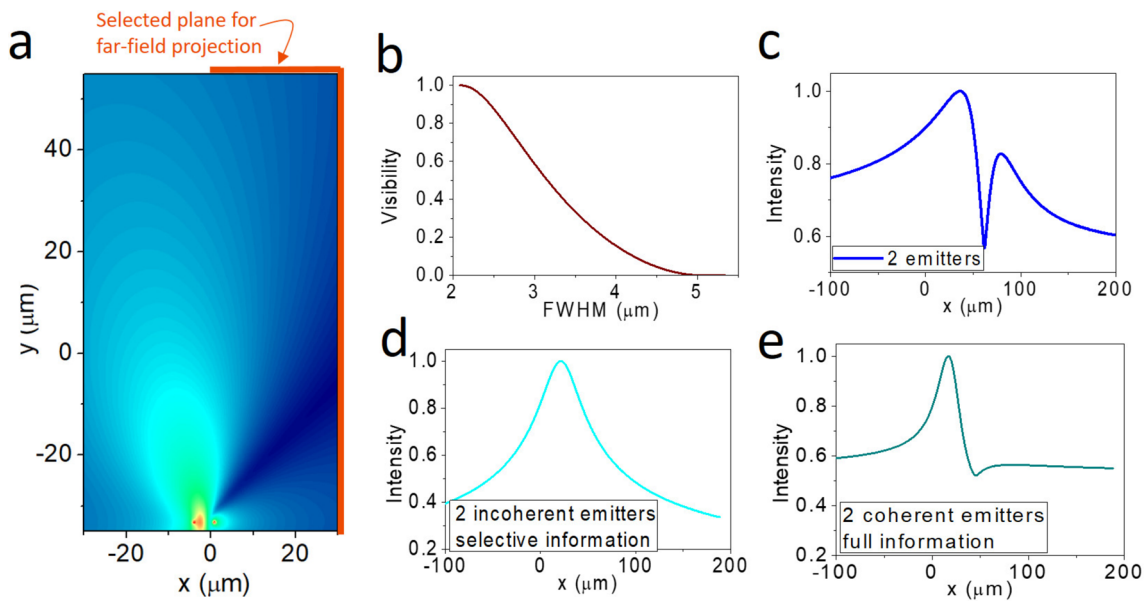


Fig. 2 CSSI of two coherent emitters. **a** Simulated intensity profile of two point sources separated by $d_0 = 4.7 \mu\text{m}$ and emitting $\lambda = 10 \mu\text{m}$. The selected plane for far-field projection is denoted as the orange line. **b** The relation between FWHM and visibility. The maximum visibility read from the far-field intensity profile is used for quantifying the FWHM. **c** The far-field (virtual image) intensity profile of two coherent emitters with $\theta_c = 80^\circ$. Here, the visibility is found to be 0.186, corresponding to $\lambda/\text{FWHM} = 2.56$. **d** The intensity profile of the virtual image for two incoherent emitters and imaging with selected information. **e** The intensity profile of the virtual image for two coherent emitters with $\theta_c = 80^\circ$ using full information

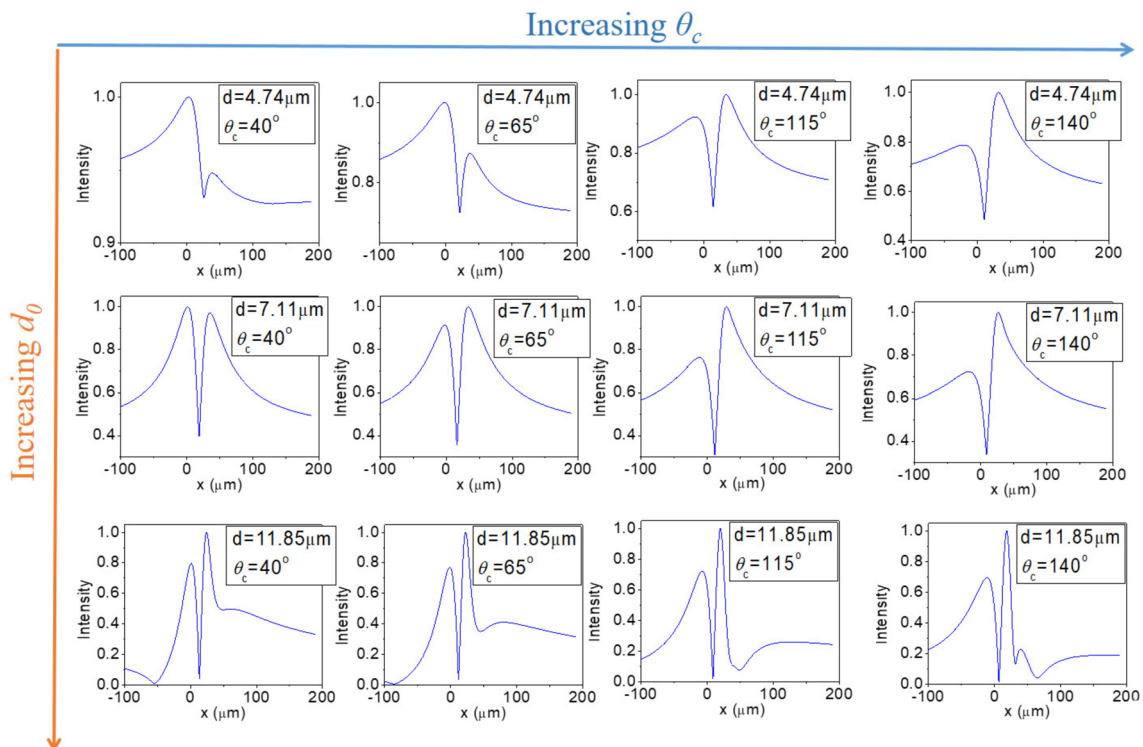


Fig. 3 Simulated far-field (virtual image) intensity profile of two point sources emitting $\lambda = 10 \mu\text{m}$ for various d_0 's and θ_c 's. Note that image speckles would appear once d_0 or θ_c becomes too large

asymmetry is a common phenomenon for CSSI. Lastly, when d_0 or θ_c becomes too large, image speckles could appear once the condition for the second destructive interference is satisfied (i.e., $2\pi nd \sin\theta/\lambda + \theta_c = 3\pi$).

3.3 Simulation of CSSI from five emitters

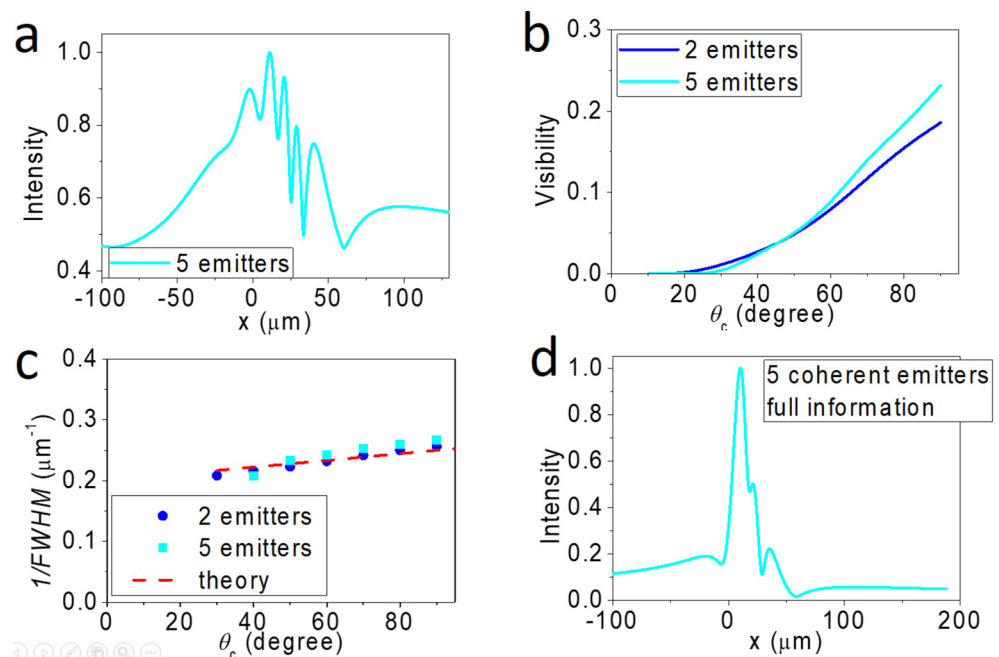
The above statements still hold for an array of point emitters with nearest neighbor $\theta_c = 80^\circ$. As demonstrated in Fig. 4a, five intensity peaks are observed, in agreement with the number of source emitters. We find that the visibility improves with increasing θ_c and the trend is nearly independent of the number of emitters, as shown in Fig. 4b. In general, the far-field profile can correctly resolve the number of point sources even though the intensity distributions may be inhomogeneous and the FWHM may be uneven. If choosing the maximum visibility in an intensity profile to represent the best FWHM, we find our simulations quantitatively agree with Eq. (5), as shown in Fig. 4c. On the other hand, controlled simulations using a full zone always fail to resolve the number of emitters, as shown in Fig. 4d.

3.4 Simulation of CSSI from coherent emitters underneath a lens

We now discuss whether it is possible to enhance the spatial resolution further. Since the discovery of superresolution assisted by dielectric microlenses [42, 43], it has been shown that microlenses exhibiting diameters less than $\sim 140\lambda$ would exhibit properties such as resolving power or magnification deviating from those of ordinary solid immersion lenses (with diameters larger than 200λ) [43–49]. The deviation becomes more pronounced when their diameters are less than 20λ . Many mechanisms have been put forward to explain the observed superresolution [43, 50–54], but there are still some fundamental disagreements. For example, a sharply focused spot (dubbed "photonic nanojet") formed at the focal point of a microlens has been frequently suggested to be the mechanism for the superresolution [43–47]. However, numerical simulations and experimental studies found the width of the nanojet to be $\sim \lambda/2$, disagreeing with many observations [48, 49]. Later, it was suggested that a resonant nanojet with a narrower width ($\lambda/3 - \lambda/4$) would appear once the incident light satisfies the condition of whisper gallery mode of a microsphere [51, 55, 56]. However, the resonant condition is difficult to meet, and it can be easily destroyed once the geometry of the lens deviates from a perfect sphere. In fact, none of the previous simulations can reproduce resolution better than $\lambda/4$, disagreeing with many experimental results.

Inspired by these works, we employ a dielectric lens for imaging coherent thermal radiation under a selected zone. Figure 5a illustrates the intensity profile of two coherent thermal radiators emitting $\lambda = 10 \mu\text{m}$ with $\theta_c = 60^\circ$. The two emitters are separated by $d_0 = 4.74 \mu\text{m}$, located underneath a $63 \mu\text{m}$ of diameter microlens with refractive index $n = 1.5$. Comparing with Fig. 2a, we find that it resolves the two emitters with better contrast even though the θ_c is smaller here. As shown in Fig. 5b, we have also simulated the results of five coherent thermal radiators emitting

Fig. 4 Simulated results of five point sources separated by $d_0 = 4.7 \mu\text{m}$ and emitting $\lambda = 10 \mu\text{m}$. **a** Simulated far-field (virtual image) intensity profile of five point sources with nearest neighbor $\theta_c(O_1-O_2) = 80^\circ$. Here, the highest visibility is found to be 0.232, corresponding to $\lambda/\text{FWHM} = 2.5$. **b** Far-field (virtual image) visibility vs. θ_c for two- (blue curve) and five- (cyan curve) point emitters. **c** The corresponding $1/\text{FWHM}$ vs. θ_c for the data shown in **b**. The theoretical prediction of Eq. (5) is shown as the red dashed line. **d** The virtual image of controlled simulation of five coherent emitters ($\theta_c = 80^\circ$) using full information



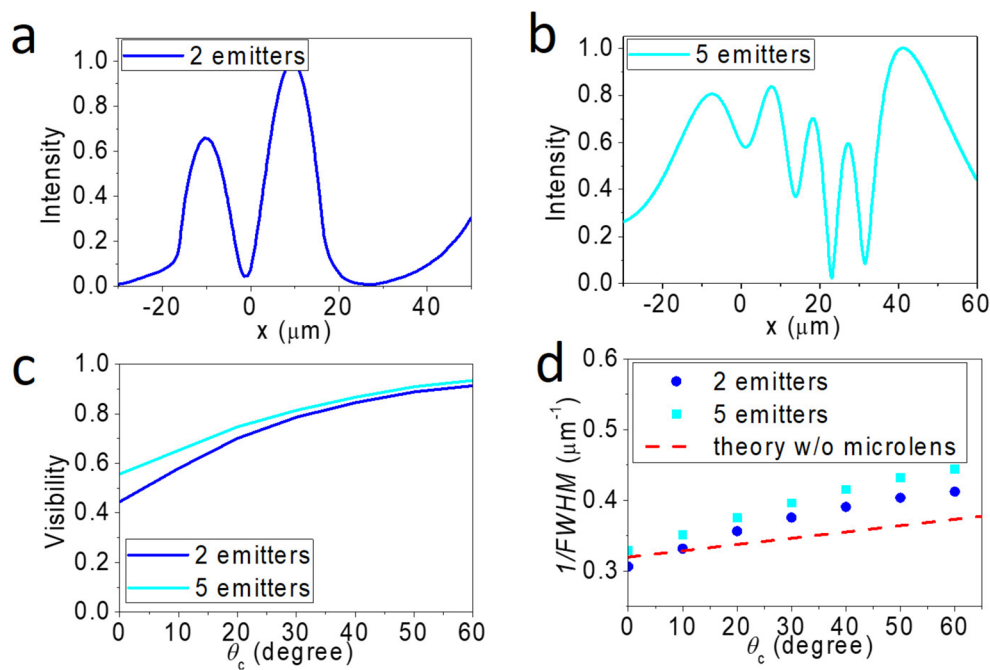


Fig. 5 Simulated far-field (virtual image) intensity profile of coherent emitters with $\theta_c(O_1-O_2)=60^\circ$, separated by $d_0=4.7 \mu\text{m}$, and emitting $\lambda=10 \mu\text{m}$ under a dielectric lens with $n=1.5$ and diameter= $63 \mu\text{m}$. **a** Simulated far-field (virtual image) intensity profile of two emitters. Here, the visibility is found to be 0.91, corresponding to $\lambda/\text{FWHM}=4.13$. **b** Simulated far-field (virtual image) intensity profile of five emitters. Here, the highest visibility is found to be 0.93, corresponding to $\lambda/\text{FWHM}=4.15$. **c** Far-field visibility vs. θ_c for two- (blue curve) and five- (cyan curve) point emitters under a $n=1.5$ dielectric lens. **d** The corresponding $1/\text{FWHM}$ vs. θ_c for the data shown in **c**. The theoretical prediction of Eq. (5) (using $NA=1.5$) is shown as the red dashed line

$\lambda=10 \mu\text{m}$ with $\theta_c=60^\circ$. It clearly resolves the five emitters with an inhomogeneous intensity distribution. Similar to Fig. 4b, Fig. 5c shows the visibility increases with increasing θ_c . Here, the highest visibility is found to be 0.93, corresponding to $\lambda/\text{FWHM}=4.15$.

To investigate the effect of the microlens, we plot the simulated data into $1/\text{FWHM}$ vs. θ_c and compare them with the prediction of Eq. (5). From Fig. 5d, we find that the presence of a microlens makes $1/\text{FWHM}$ versus θ_c relation deviate from Eq. (5) and the $1/\text{FWHM}$ increases with a higher slope than the prediction of Eq. (5). Besides, the slope is steeper for the five-point emitters than that for the two-point emitters. Because of the linear relation shown in Fig. 5d, we empirically introduce an enhanced factor f to account for the effective phase difference ($f\theta_c$) observed in the microlens. Apparently, f would be a complex function of the number of emitters, their locations, the n of the microsphere, and the diameter of the microsphere. Although investigating the physics behind f is beyond the scope of the paper, we have learned that the overall effect of introducing the microsphere can be simplified to a single parameter f .

We now discuss possible scenarios that can implement CSSI. The θ_c of coherent thermal radiation can be created by applying a temperature gradient along a polar material, in which an added heat flux has been experimentally observed [57]. Alternatively, CSSI can be used for imaging samples deposited on a metasurface with surface plasmons or surface phonon-polaritons excited by lasers or other external light sources [58–61]. In general, θ_c can always be created once there are interactions between two sources. On the other hand, because selecting the correct information zone will give better resolution than the other in 1D cases, one can easily carry out CSSI by tilting/rotating the sample, changing the direction of the temperature gradient, or varying the incident angle of an external light source. Because the concept introduced here is simple and does not incorporate any quantum [62–66] or nonlinear effects [67, 68], we anticipate that the technique can be extended to 2D imaging. For example, similar to the methods used in structural illumination, CSSI in 2D can be carried out by rotating the sample or the external light source. Image speckles can be removed by using an algorithm that compares CSSI with images from incoherent light sources or employs full information.

4 Conclusion

In conclusion, existing superresolution techniques generally assume that higher spatial resolution can be achieved by utilizing the maximum information received in the far field. Here, we provide a counterexample demonstrating that spatial resolution going beyond the Abbe diffraction limit can be obtained in the far field when sources emit coherent light and only selective information is used for imaging. This concept may be realized using coherent thermal radiation mediated by surface phonon polaritons. Additionally, we show that spatial resolution can be further enhanced by introducing a dielectric microsphere to the system. Thus, beyond thermal imaging, this new technique may inspire advancements in infrared microscopy, such as Fourier transform infrared spectroscopy.

Acknowledgements C.W.C. thanked Bo-Yi Chen's help during the revision when D.H.H. left and was uncooperative. This work was supported by the Ministry of Science and Technology of Taiwan (MOST 104-2628-M-002-010-MY4 and 102-2112-M-002-018-MY3).

Author contributions CWC initiated the project. DHH conducted the simulation and the analysis. CWC wrote the paper. All authors discussed the results and commented on the manuscript.

Data availability The data supporting the findings of this study are available within the paper and its supplementary information file.

Declarations

Competing interests The authors declare no that they have no competing interests.

Open Access This article is licensed under a Creative Commons Attribution 4.0 International License, which permits use, sharing, adaptation, distribution and reproduction in any medium or format, as long as you give appropriate credit to the original author(s) and the source, provide a link to the Creative Commons licence, and indicate if changes were made. The images or other third party material in this article are included in the article's Creative Commons licence, unless indicated otherwise in a credit line to the material. If material is not included in the article's Creative Commons licence and your intended use is not permitted by statutory regulation or exceeds the permitted use, you will need to obtain permission directly from the copyright holder. To view a copy of this licence, visit <http://creativecommons.org/licenses/by/4.0/>.

References

1. Gabriel WF. Spectral-analysis and adaptive array superresolution techniques. *Proc IEEE*. 1980;68:654–66.
2. Groetsch CW. Integral equations of the first kind, inverse problems and regularization: a crash course. *J Phys Conf Ser*. 2007;73: 012001.
3. Linfoot EH. Information theory and optical images. *J Opt Soc Am*. 1955;45:808–19.
4. Linfoot EH. Resolving power and information. *J Opt Soc Am*. 1956;46:72–72.
5. Harris JL. Diffraction + resolving power. *J Opt Soc Am*. 1964;54:931.
6. Rushforth CK, Harris RW. Restoration resolution and noise. *J Opt Soc Am*. 1968;58:539.
7. Bershada NJ. Resolution optical-channel capacity and information theory. *J Opt Soc Am*. 1969;59:157–60.
8. Kosarev EL. Shannon superresolution limit for signal recovery. *Inverse Probl*. 1990;6:55–76.
9. den Dekker AJ, vanden Bos A. Resolution: a survey. *J Opt Soc Am A*. 1997;14:547–57.
10. Narimanov E. Resolution limit of label-free far-field microscopy. *Adv Photonics*. 2019;1:056003.
11. Astratov VN, et al. Roadmap on label-free super-resolution imaging. *Laser Photonics Rev*. 2023;17:2200029.
12. Hell SW, et al. The 2015 super-resolution microscopy roadmap. *J Phys D Appl Phys*. 2015;48:443001.
13. Lukosz W, Warga ME. Optical systems with resolving powers exceeding the classical limit. *J Opt Soc Am*. 1966;56:548–50.
14. Lukosz W. Optical systems with resolving powers exceeding classical limit. *J Opt Soc Am*. 1967;57:932.
15. Cox IJ, Sheppard CJR. Information capacity and resolution in an optical-system. *J Opt Soc Am A*. 1986;3:1152–8.
16. Cox IJ, Sheppard CJR. The information capacity of a multidimensional communications-system. *Int J Electron*. 1986;60:655–62.
17. Gustafsson MGL. Surpassing the lateral resolution limit by a factor of two using structured illumination microscopy. *J Microsc*. 2000;198:82–7.
18. Rogers ETF, et al. A super-oscillatory lens optical microscope for subwavelength imaging. *Nat Mater*. 2012;11:432–5.
19. Lu DL, Liu ZW. Hyperlenses and metalenses for far-field super-resolution imaging. *Nat Commun*. 2012;3:1205.
20. Liu ZW, Lee H, Xiong Y, Sun C, Zhang X. Far-field optical hyperlens magnifying sub-diffraction-limited objects. *Science*. 2007;315:1686–1686.
21. Pu T, Ou JY, Papisimakis N, Zheludev NI. Label-free deeply subwavelength optical microscopy. *Appl Phys Lett*. 2020;116:131105.
22. Pu TC, et al. Unlabeled far-field deeply subwavelength topological microscopy (DSTM). *Adv Sci*. 2021;8:2002886.
23. Goodman JW. Introduction to Fourier optics. 3rd ed. Greenwood Village: Roberts & Co.; 2005.
24. Helmchen F, Denk W. Deep tissue two-photon microscopy. *Nat Methods*. 2005;2:932–40.
25. Hsu KJ, Lin YY, Chiang AS, Chu SW. Optical properties of adult brains in one-, two-, and three-photon microscopy. *Biomed Opt Express*. 2019;10:1627–37.
26. Rubinsztein-Dunlop H, et al. Roadmap on structured light. *J Opt*. 2017;19:013001.
27. Jacob Z, Alekseyev LV, Narimanov E. Optical hyperlens: far-field imaging beyond the diffraction limit. *Opt Express*. 2006;14:8247–56.

28. Greffet JJ, et al. Coherent emission of light by thermal sources. *Nature*. 2002;416:61–4.
29. Dahan N, Niv A, Biener G, Kleiner V, Hasman E. Space-variant polarization manipulation of a thermal emission by a SiO subwavelength grating supporting surface phonon-polaritons. *Appl Phys Lett*. 2005;86: 191102.
30. Laroche M, et al. Highly directional radiation generated by a tungsten thermal source. *Opt Lett*. 2005;30:2623–5.
31. Laroche M, Carminati R, Greffet JJ. Coherent thermal antenna using a photonic crystal slab. *Phys Rev Lett*. 2006;96: 123903.
32. Liu XL, et al. Taming the blackbody with infrared metamaterials as selective thermal emitters. *Phys Rev Lett*. 2011;107: 045901.
33. Guo Y, Cortes CL, Molesky S, Jacob Z. Broadband super-Planckian thermal emission from hyperbolic metamaterials. *Appl Phys Lett*. 2012;101: 131106.
34. Burckel DB, Davids PS, Finnegan PS, Figueiredo PN, Ginn JC. Directional emissivity from two-dimensional infrared waveguide arrays. *Appl Phys Lett*. 2015;107: 121902.
35. Hajian H, Ghobadi A, Butun B, Ozbay E. Nearly perfect resonant absorption and coherent thermal emission by hBN-based photonic crystals. *Opt Express*. 2017;25:31970–87.
36. Duggan R, Ra'di Y, Alù A. Temporally and spatially coherent emission from thermal embedded eigenstates. *ACS Photonics*. 2019;6:2949–56.
37. Shin SM, Elzouka M, Prasher R, Chen RK. Far-field coherent thermal emission from polaritonic resonance in individual anisotropic nanoribbons. *Nat Commun*. 2019;10:1377.
38. Bailly E, et al. 2D silver-nanoplatelets metasurface for bright directional photoluminescence, designed with the local Kirchhoff's law. *ACS Nano*. 2024;18:4903–10.
39. Fan ZW, Hwang T, Lin S, Chen YX, Wong ZJ. Directional thermal emission and display using pixelated non-imaging micro-optics. *Nat Commun*. 2024;15:4544.
40. Baranov DG, et al. Nanophotonic engineering of far-field thermal emitters. *Nat Mater*. 2019;18:920–30.
41. Yu LY, Cyue ZR, Su GD. Three-stage full-wave simulation architecture for in-depth analysis of microspheres in microscopy. *Opt Express*. 2020;28:8862–77.
42. Lee JY, et al. Near-field focusing and magnification through self-assembled nanoscale spherical lenses. *Nature*. 2009;460:498–501.
43. Wang Z, et al. Optical virtual imaging at 50 nm lateral resolution with a white-light nanoscope. *Nat Commun*. 2011;2:218.
44. Chen ZG, Taflove A, Backman V. Photonic nanojet enhancement of backscattering of light by nanoparticles: a potential novel visible-light ultramicroscopy technique. *Opt Express*. 2004;12:1214–20.
45. Itagi AV, Challener WA. Optics of photonic nanojets. *J Opt Soc Am A*. 2005;22:2847–58.
46. Lecler S, Takakura Y, Meyrueis P. Properties of a three-dimensional photonic jet. *Opt Lett*. 2005;30:2641–3.
47. Devilez A, et al. Three-dimensional subwavelength confinement of light with dielectric microspheres. *Opt Express*. 2009;17:2089–94.
48. Heifetz A, et al. Experimental confirmation of backscattering enhancement induced by a photonic jet. *Appl Phys Lett*. 2006;89: 221118.
49. Ferrand P, et al. Direct imaging of photonic nanojets. *Opt Express*. 2008;16:6930–40.
50. Ben-Aryeh Y. Superresolution observed from evanescent waves transmitted through nano-corrugated metallic films. *Appl Phys B*. 2012;109:165–70.
51. Geints YE, Zemlyanov AA, Panina EK. Photonic jets from resonantly excited transparent dielectric microspheres. *J Opt Soc Am B*. 2012;29:758–62.
52. Duan Y, Barbastathis G, Zhang B. Classical imaging theory of a microlens with super-resolution. *Opt Lett*. 2013;38:2988–90.
53. Cang H, Salandrino A, Wang Y, Zhang X. Adiabatic far-field sub-diffraction imaging. *Nat Commun*. 2015;6:7942.
54. Fan W, Yan B, Wang ZB, Wu LM. Three-dimensional all-dielectric metamaterial solid immersion lens for subwavelength imaging at visible frequencies. *Sci Adv*. 2016;2:e1600901.
55. Heifetz A, Simpson JJ, Kong SC, Taflove A, Backman V. Subdiffraction optical resolution of a gold nanosphere located within the nanojet of a Mie-resonant dielectric microsphere. *Opt Express*. 2007;15:17334–42.
56. Lee S, Li L, Wang Z. Optical resonances in microsphere photonic nanojets. *J Opt*. 2014;16: 015704.
57. Wu Y, et al. Enhanced thermal conduction by surface phonon-polaritons. *Sci Adv*. 2020;6:eabb4461.
58. Giles AJ, et al. Ultralow-loss polaritons in isotopically pure boron nitride. *Nat Mater*. 2018;17:134.
59. Ma WL, et al. In-plane anisotropic and ultra-low-loss polaritons in a natural van der Waals crystal. *Nature*. 2018;562:557.
60. Dong Y, et al. Fizeau drag in graphene plasmonics. *Nature*. 2021;594:513.
61. Zhao WY, et al. Efficient Fizeau drag from Dirac electrons in monolayer graphene. *Nature*. 2021;594:517.
62. Nair R, Tsang M. Far-field superresolution of thermal electromagnetic sources at the quantum limit. *Phys Rev Lett*. 2016;117:190801.
63. Paúr M, Stoklasa B, Hradil Z, Sánchez-Soto LL, Rehacek J. Achieving the ultimate optical resolution. *Optica*. 2016;3:1144–7.
64. Tsang M, Nair R, Lu XM. Quantum theory of superresolution for two incoherent optical point sources. *Phys Rev X*. 2016;6:031033.
65. Tham WK, Ferretti H, Steinberg AM. Beating Rayleigh's curse by imaging using phase information. *Phys Rev Lett*. 2017;118:070801.
66. Liang K, Wadood SA, Vamivakas AN. Coherence effects on estimating two-point separation. *Optica*. 2021;8:243–8.
67. Duh YS, et al. Giant photothermal nonlinearity in a single silicon nanostructure. *Nat Commun*. 2020;11:4101.
68. Zhou ZH, et al. Far-field super-resolution imaging by nonlinearly excited evanescent waves. *Adv Photonics*. 2021;3:025001.

Publisher's Note Springer Nature remains neutral with regard to jurisdictional claims in published maps and institutional affiliations.

Supplementary information for Superresolution based on coherent thermal radiation with selective information

Duan-Hsin Huang,¹ and Chih-Wei Chang^{1,2}

¹Center for Condensed Matter Sciences, National Taiwan University, Taipei 10617, Taiwan

²Center of Atomic Initiative for New Materials (AI-MAT), National Taiwan University, Taipei, 10617, Taiwan

S1. Visibility vs FWHM. Figure S1 shows a representative intensity profile at the image plane at the far field. For each local intensity maximum and minimum, we can calculate its visibility = $(I_{max}-I_{min})/(I_{max}+I_{min})$. The maximum visibility is chosen to calculate the FWHM in Fig. S1 and in the main text.

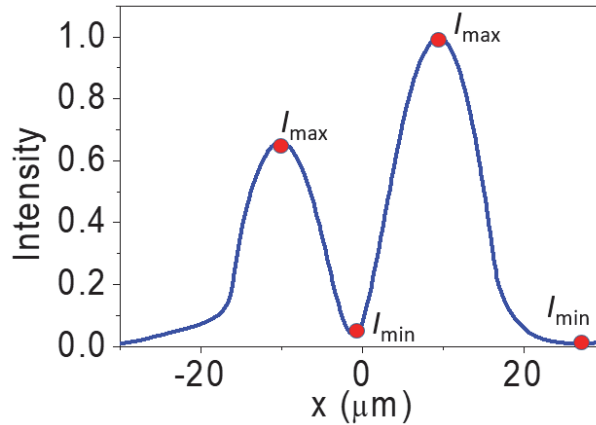


Figure S1. A representative intensity profile of the image plane at the far field. The local intensity maximums and minimums are denoted as red circles. Maximum visibility is chosen to plot the relation between FWHM and visibility in the main text figures.

The deconvolution method is obtained by reading the maximum visibility of the far-field intensity and using Fig. 2(b) in the main text to obtain the FWHM. The relation between visibility and FWHM is established using the procedures described in Fig. S2. First, the FWHM of a point source emitting a wavelength (λ) is directly obtained from its far-field intensity profile. Then, another point source emitting identical λ but separated from the first point source by $d_0=4.7 \mu\text{m}$ and $\theta_c=90^\circ$ is added to the simulation. From the far-field intensity profile shown in Fig. S2(b), we can obtain its visibility. Because the capability of identifying an intensity minimum is usually used as Abbe's (and also Rayleigh's) criteria for defining the resolution limit for two-point emitters,

the visibility or the FWHM can be used for quantification of an optic system. Lastly, the above procedures are repeated for different λ 's and the relation between FWHM and visibility is established, as shown in Fig. S2(c).

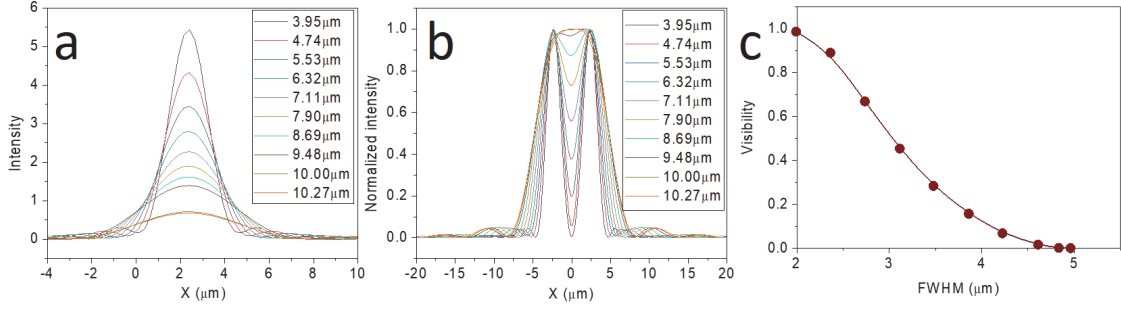


Figure S2. The relation between FWHM and visibility. (a) The simulated far-field intensity profile of a point source emitting different λ 's. The FWHM is directly read from each profile. (b) The far-field intensity profile of two incoherent sources emitting different λ 's. Here, the visibility can be directly determined using the method shown in Fig. S1. (c) The established relation between FWHM and visibility, where the data points are from (a) & (b) and the brown curve is from Fig. 2(b).

S2. Controlled simulations: incoherent imaging and imaging with full information.

To prove that coherent imaging and selective information at the image plane are the two key factors of CSSI, we provide controlled simulations for incoherent imaging and coherent imaging with full information capacity, respectively shown in Figs. S3(a & b).

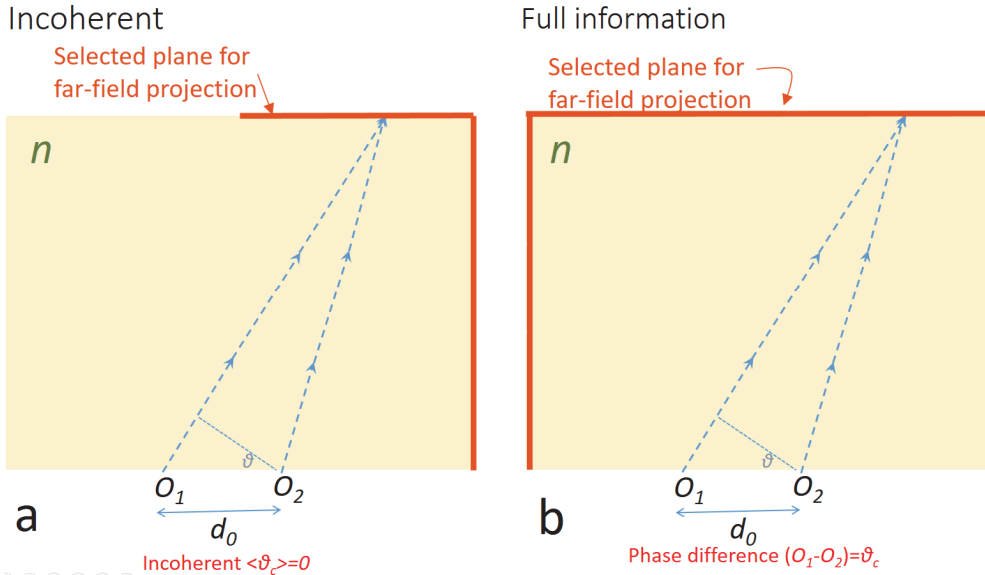


Figure S3. Schematic illustrations of two point sources (denoted by O_1 and O_2 , immersed in a media of refractive index n) that are imaged using (a) incoherent imaging with selective information and (b) coherent imaging with full information.